<u>DATA REPOSITORY:</u> Berger and Spotila, in rev., "Denudation and Deformation of a Glaciated Orogenic Wedge: The St. Elias Orogen, Alaska"

APPENDIX DR-1: Thermochronologic methods

Low-temperature thermochronometry was used to constrain the exhumation pattern across the St. Elias orogen. New (U-Th)/He ages of apatite (AHe) were obtained from bedrock samples collected by helicopter along the east-west ELA front along the windward flank of the orogen. Samples used consisted mainly of sedimentary (arkose, graywacke) and metamorphic (gneiss) lithologies. New ages were combined with previous AHe ages from Spotila et al. (2004) and Berger et al (in press). (U-Th)/He is based on the radiogenic production and thermally-controlled diffusion of ^{4}He within host minerals. Apparent AHe cooling ages typically correspond to closure temperatures of ~70 ˚C, but closure temperature is cooling-rate and grain-size dependent (Wolf et al., 1996; Farley, 2000; Ehlers and Farley, 2003).

AHe ages were measured at Virginia Tech on 1-25 grain, ~0.01-0.03 mg aliquots (Table DR-1). Apatite grains dated were ≥70 μm in diameter and were screened for microinclusions and other crystal defects at 100x magnification. Although the highest quality apatite grains available were used, apatite yields from some samples were poor, forcing the use of lower-quality grains. To counter the potential effect of U- and Th-bearing microinclusions (i.e. zircon and monazite (House et al., 1997)), fluid inclusions, or parent nuclide zonation on measured ages (Fitzgerald et al., 2006), we analyzed multiple (~5) replicates per sample (a total of 97 analyses for 19 samples). This enabled evaluation of sample reproducibility and identification of anomalously old outliers that

likely have ^{4}He contamination. Samples were outgassed in Pt tubes in a resistance furnace at 940 ˚C for 20 minutes (followed by a 20-minute reextraction test) and analyzed for ^{4}He by isotope dilution utilizing a ^{3}He spike and quadrupole mass spectrometry. Blank levels for ^{4}He detection using current procedures at Virginia Tech are ~0.2 femtomoles. Radiogenic parent isotopes (^{238}U, ^{235}U, and ^{232}Th) were measured at Yale University and Caltech using isotope dilution (^{235}U and ^{230}Th spike) and ICP mass spectrometry. Although ^{4}He is also produced by ^{147}Sm decay, it was not routinely measured because it should produce <1% of radiogenic ^{4}He in typical apatite and should only be a factor in AHe ages when U concentrations are <5 ppm (which applies to none of our samples; Table DR1) (Farley and Stockli, 2002; Reiners and Nicolescu, in press).

Routine 1σ uncertainties due to instrument precision are ±1-2% for U and Th content, ±2-3% for He content, and ±4-5% for alpha ejection correction factor based on grain dimension and shape. Cumulative analytical uncertainty is thus approximately ±10% (2σ). Age accuracy was cross-checked by measurements of known standards, such as Durango fluorapatite (30.9±1.53 Ma (1σ; n=40)), with a known age of 31.4 Ma (McDowell et al., 2005)). These measurements on Durango show that reproducibility on some natural samples is comparable to that expected from analytical errors.

Uncertainties for samples are reported as the observed standard deviation from the mean of individual age determinations (Table DR-1). The average AHe reproducibility on well-reproduced average ages is ~11% (1σ; 16 samples, 74 age determinations), which is worse than that obtained from Durango apatite. Some samples with very young average AHe ages reproduced well, such as 05STP2 (0.44 Ma ±6.9% 1σ, n=5) and 05STP4 (0.74 Ma ±9.7% 1σ, n=6). Other samples reproduced more poorly. The 11%

average reproducibility excludes three samples (05STP11, 06STP1, 06STP71) that reproduced poorly (1σ>20%). Two of these samples are from thin Cenozoic stratigraphy on the eastern end of the orogen and may be only partially reset (see below). The 11% average reproducibility also ignores ten individual age determinations that were considered outliers and culled prior to calculation of average age, because they were significantly older than concordant replicates and were likely contaminated by excess ^{4}He due to inclusions (Table DR-1).

The pattern of new ages measured here are consistent with previous AHe dating in the orogen (Spotila et al., 2004; Berger et al., in rev.) (Fig. 1). One sample dated here was also dated previously by Spotila et al. (2004), but with a discrepant result. Sample 02CH28 was reported as average AHe of 4.8 Ma by Spotila et al. (2004), but was redated here as 0.73 Ma (Table DR-1). One of four new age determinations was anomalously old (Table DR-1), suggesting this sample is prone to ^{4}He contamination by micro-inclusions. Although there is no independent indication that the earlier analyses were inaccurate due to poor apatite quality, we choose to use the younger age population (i.e. the new data) for our interpretations here (Fig. 1).

AHe ages constrain the pattern of low-temperature cooling throughout most of the orogen (Fig. 1). However, many of the samples that reproduced poorly are from the eastern part of the orogen, near the bend in the plate boundary at the Fairweather fault and the Seward and Hubbard outlet glaciers. One sample from near the Hubbard glacier is very young (06STP4, 0.56 Ma), but other samples from this region do not yield reproducible ages. This may be because these Cenozoic sedimentary samples were not buried deeply enough to be completely reset. The stratigraphic cover of the Yakutat

terrane is thinner on the east than on the west, and if these sample were exhumed from very shallow depths, some detrital grains may retain pre-depositional ^{4}He. As a result, two of the resulting average ages (06STP71 and 06STP3) were not used for the contours on Fig. 1 and were excluded from the regression plot in Fig. 2b.

For the purposes of this study, we primarily focus on differences in apparent cooling ages, rather than estimates of exhumation rate. Assuming geothermal and topographic conditions are more or less uniform across the orogen, the 50-fold difference in cooling ages across the orogen should represent major differences in exhumation rate. However, it is still useful to consider what exhumation rates these young AHe ages may correspond to. Given the rapid cooling, a closure temperature approach is a suitable approximation for estimating exhumation rate. Closure temperatures for these rapidly-cooled samples should vary from ~70-90 ˚C, based on sample grain sizes and standard apatite diffusion parameters (Farley, 2000). Based on regional estimates of geothermal gradient in the absence of rapid denudation of 25 ˚C/km (Magoon, 1986; Johnsson et al., 1992; Johnsson and Howell, 1996), this range in closure temperature should correspond to closure depths of 2.8-3.6 km. However, it is likely that heat is advected due to rapid exhumation, such that the geothermal gradient is steeper. Using the 1-dimensional, steady-state thermokinematic solution to the crust's thermal profile from Reiners and Brandon (2006), the geothermal gradient could be elevated to ~46 ˚C/km if denudation rates are as high as 5 mm/yr, assuming reasonable boundary conditions for the orogenic wedge (layer thickness (L) of 10 km (the maximum stratigraphic thickness above subducting Eocene oceanic crust of the accreting Yakutat terrane (Plafker et al., 1994)), and thermal parameters from Reiners and Brandon (2006) of thermal diffusivity $\kappa = 27.4$

93 km^2/Ma, surface temperature T_S = 0 ˚C, basal temperature T_L = 250 ˚C (for regional
94 geothermal gradient of 25 ˚C/km), and internal heat production H_T = 4.5 ˚C/Ma). Thisx
95 approach assumes that fluid convection does not influence isotherm depth. Using this
96 elevated geothermal gradient, AHe closure depths for the area of rapid cooling are 1.5-2
97 km, such that AHe contours of 0.5, 0.75, and 1.0 Ma on Fig. 1 correspond to maximum
98 time-averaged exhumation rates of 4.0, 2.7, and 2.0 mm/yr. This elevated geothermal
99 gradient was also used for the exhumation rates in Fig. 3.

100 Such rapid rates of exhumation are consistent with a poorly-defined age-elevation
101 gradient from a near-vertical sample transect from just west of the Bering glacier. Three
102 samples from Khitrov ridge define a very rough age-elevation gradient of 0.144 Ma/km
103 (6.9 mm/yr) between 0.44 and 0.53 Ma (Fig. DR-1). The zero-age intercept of this
104 gradient occurs at 2.5 km below sea level, which given the ~0.5 km mean elevation of the
105 area corresponds to ~3.0 km below the surface. The rate of exhumation required to bring
106 the bottom sample to the surface from this depth is 6.8 mm/yr, such that the gradient and
107 the intercept are mutually consistent. Using a closure temperature for these samples of
108 ~88 ˚C, calculated iteratively based on grain size, diffusion characteristics (Farley, 2000),
109 and the resulting cooling rate, the inferred geothermal gradient is 29 ˚C/km. This implies
110 even faster exhumation than estimated using the 1-dimensional model and 46 ˚C/km
111 geothermal gradient. Age-elevation gradients can be affected by variations in isotherm
112 shape associated with topography. Calculations by Mancktelow and Grasemann (1997)
113 for a case of similar relief (1.5 km), topographic wavelength (~5 km), geothermal
114 gradient (~35˚ C/km), closure temperature (100 ˚C), and exhumation rate (5 mm/yr),
115 suggest that the age-elevation gradient could overestimate the exhumation rate by ~20%.

Given that the age-elevation gradient is poorly defined and likely overestimates exhumation rate, we use the result from the 1-dimensional model for our interpretations. However, this relief transect at least corroborates that exhumation rates in the area are very rapid.

Other effects of sample elevation and topography are not likely to alter the first order patterns of exhumation we infer for this area. Samples were generally collected from ridge tops of comparable relief (~1-2 km) by helicopter. This should help minimize the effect of variable isotherm shape and deviations between local sample elevation and mean topography on inferred exhumation rates. In addition, given the typical 10-km-wavelength relief of ~1-2 km for most of the area (higher-relief parts of the orogen have not been sampled; Fig. 1), the maximum difference in closure depths between locations should be less than a factor of two, which cannot account for the ~50-fold difference in ages from north to south or the ~5-fold difference within the rapidly-cooled windward flank. Based on this, we interpret the pattern of AHe ages to reflect spatial variations in exhumation rate.

APPENDIX DR-2: Glaciological parameters and precipitation data

The source areas for the major southward-flowing glaciers in the St. Elias orogen were defined based on ice distributions on 1:250,000 USGS topographic maps (Fig. DR-2). Divides were drawn based on the principle that ice flows down ice gradient, such that ice divides are the highest point on a continuous ice sheet that flows into multiple glacier systems. The glacier drainage areas upstream of equilibrium line altitudes (ELA) were calculated graphically and are listed in Table DR-2. These drainage areas include

hillslopes above the glaciers and are thus larger than the surface area of ice above ELA, but are obviously only a subset of the total drainage basin of each glacier (i.e. extended to the glacier termini). Given that the maps used were in some cases decades old, and the fact that glaciers have receded in much of this region over the past century (Porter, 1989), the ice distributions and ELA shown should be considered approximate 20th century conditions.

Modern glacier ELAs were determined for large and small windward-flowing glaciers on the basis of topographic contours of the glacier surfaces from 1:250,000 scale USGS maps. ELAs for the glaciers shown in Figs. 1 and DR-2 are listed in Table DR-2. This method is based on defining the boundary between accumulation and ablation areas on the glacier, where accumulating regions have concave contours and ablation areas have convex contours in the direction of glacier flow (Meierding, 1982; Mayo, 1986; Benn and Lehmkuhl, 2000). This technique is simple and can be performed using only topographic maps over a wide area, but provides only an approximation of true ELA. It is less accurate than other approaches, such as using field or airphoto observations of snowcover during the melt season, smaller glaciers, or other meteorological data. The accumulation area ratio (AAR) technique could not be used, given that many glaciers flow directly into the ocean and experience ice removal by calving. However, the results obtained are consistent with regional syntheses of modern ELA (Péwé, 1975; Mayo, 1986).

More precise determination of modern ELAs would not enhance the comparison to AHe ages, given that uncertainties in paleo-ELAs are much larger (see below) and because ELAs should fluctuate significantly even at decadal timescales. Glaciers exhibit

a prolonged response, called physical memory, to cyclic variations in precipitation in the absence of climate change (e.g. Pacific Decadal Oscillation), such that ELAs may routinely shift horizontally by up to several kilometers (Roe and O'Neal, in prep.). More recent airphotos and satellite imagery would also be affected by the rapid glacial retreat that has occurred in Alaska over the past few decades, and may thus not represent typical interglacial conditions. The use of coarse topographic maps ignore these short term fluctuations and may thus better approximate mean 20th century conditions. Nonetheless, uncertainties in the horizontal position of modern ELA are assumed to be at least $\pm$2 km.

Uncertainties in the position of paleo-ELA during glacial maxima periods outweigh errors in the position of modern ELA. Paleo-ELA is not well constrained along the windward flank of the orogen, given post-glacial-maximum erosion and deposition on the continental margin. We assumed ELA was ~300 m lower along the coast during glacial maxima, based on regional estimates (Péwé, 1975). ELAs during glacial maxima are not well constrained, however, and may have fluctuated throughout the Quaternary (e.g. the Illinoan glacial maximum ELA was lower than the last glacial maximum ELA; Péwé, 1975). This assumption of paleo-ELA provides a weak lower bound of what we define as the "ELA front", or the zone lying between modern and glacial-maxima ELA on the windward flank of the orogen. Based on errors in the elevation of paleo-ELA of at least $\pm$100 m and because of the gentle slope of the coastal plain, we assign $\pm$5 km horizontal uncertainty to the lower bound of the ELA front.

We compare these glaciological parameters to bedrock cooling and exhumation in several ways. The comparison between AHe age distribution and the position of the ELA front (Figs. 1, 2) should test how time-averaged, long-term denudation is associated with

the zone of theoretically-greatest ice flux and erosion on individual glaciers (Andrews, 1972; Hallet, 1979; Anderson et al., 2006). This comparison is only approximate, however, given that the position of ELAs during glacial maxima are poorly constrained and that mean ELA may fluctuate due to changes in climate or topography over shorter (10^5 yr) timescales than the AHe cooling ages (10^6 yr). The comparison of long-term exhumation rates with variations in ice flux along strike is more poorly constrained (Fig. 3). Modern glacier drainage areas at ELA should only approximate relative differences in modern ice discharge between glaciers, given that precipitation varies across the area by up to a factor of two (Fig. DR-2) and due to other complicating variables which are not considered (e.g. aspect, albedo, etc.). Modern glacier drainage areas should be an even poorer representation of mean Quaternary ice discharge, given that precipitation patterns and glacier drainage divides could have varied between glacial cycles. Better constraints on the position of ELA during glacial maxima or climate-glacier flow models that predict the distribution of glaciers throughout the Quaternary would improve this comparison. Given the likelihood that outlet glaciers have been fixed during at least the last few glacial cycles by Waxell-St. Elias ridge (see below), however, it is likely that the heterogeneity in modern drainage areas at least approximates how ice discharge has varied throughout multiple glacial intervals.

Existing precipitation data for the St. Elias orogen are sparse. Estimated isohyets of mean annual precipitation based on a regional climate summary of existing precipitation data and patterns of snow lines throughout the state of Alaska are shown in Fig. DR-2 (Péwé, 1975). These isohyets have poor resolution and likely miss major spatial variations in precipitation associated with local topography. A second estimate of

mean annual precipitation is from the Spatial Climate Analysis Center (2002) (Fig. DR-2). This uses the statistical method *PRISM* (Parameter-elevation Regression on Independent Slopes Model), which combines historical point data for annual precipitation (from 1961-1990) with 2-km-resolution topography from a digital elevation model to estimate the effects of terrain on climate in mountainous regions (Daly et al., 1994). Although the PRISM precipitation data are based on similarly limited observations as Péwé (1975), we consider it more accurate because it accounts for the local effects of orography. The variation in precipitation for both sources are shown along the north-south transect (AA') in Fig. 2. Neither appears to correlate with the location of the youngest AHe ages. However, the poor constraints on precipitation in this area severely limits this comparison with AHe age distribution.

APPENDIX DR-3: Waxell-St. Elias Ridge

The zone of rapid denudation and the ELA front both occur south of a prominent east-west ridge, which forms an impressive barrier to ice flow in the St. Elias orogen. The Waxell-St. Elias ridge runs east-west, parallel to the coast, and consists of several discrete, elliptical segments that span a total of >300 km (Fig. 1, DR-3). Glaciers currently flow north to south through this barrier at only five locations, where major outlet glaciers with massive ice discharge occur (e.g. Bering and Malaspina glaciers; Figs. 1, DR-2, DR-3). During glacial maxima periods, it is likely that ice flow over this ridge occurred at only several other points, given its height relative to the probable elevation of the Bagley ice field behind it (Fig. DR-3). This means that most of the ELA

front would have been isolated from direct north to south ice flow across this barrier, thereby keeping ice discharge heterogenous along the range front during glacial maxima.

The prominent Waxell-St. Elias ridge may have also had an important influence on the pattern of glaciation and denudation in the orogen. The ridge exists partly due to motion of a backthrust under the Bagley ice field (Berger et al., in press), but is also due to the presence of very resistant bedrock (greenschist-amphibolite grade metasediment and metavolcanics; Plafker et al., 1994). As a result of this ridge, glaciers are unable to flow directly south across the orogen, resulting in just a few local outlet glaciers and considerable east-west ice flow north of the ridge (Fig. 1, DR-2). The zone of rapid denudation occurs just south of this ridge, within easily-eroded Cenozoic stratigraphy of the deforming Yakutat terrane. In contrast, the accumulation area of southward flowing outlet glaciers is floored by more resistant bedrock of the Prince William and Chugach terranes (Plafker et al., 1994). This may help facilitate denudation at the ELA front, by resisting erosion in the north, trapping ice in the Bagley ice field, forcing ice flow through narrow outlets, and perhaps even by focusing orographic precipitation and ice-avalanching on the ELA front to the south. Without the Waxell-St. Elias ridge, the glacio-erosional evolution of the orogen may have been different, thus implying that physiogeologic setting has been an important part of this orogen's history.

REFERENCES

Benn, D.I., and Lehmkuhl, F., 2000, Mass balance and equlibrium line altitudes of glaciers in high-mountain environments, Quat. Int., 65/66, 15-29.

Berger, A.L., Spotila, J.A., Chapman, J., Pavlis, T., and Enkelmann, E., in review, Architecture, kinematics, and exhumation, across the central St. Elias Orogen; A thermochronologic approach, Earth. and Planet. Sci. Lett.

Daly, C., Neilson, R.P., and Phillips, D.L., 1994, A statistical-topographic model for mapping climatological precipitation over mountainous terrain, Journal of Applied Meteorology, 33, 140-158.

Ehlers, T., and Farley, K., 2003, Apatite (U-Th)/He thermochronometry: methods and applications to problems in tectonics and surface processes, Earth and Planetary Science Letters, 206, 1-14.

Farley, K.A., 2000, Helium diffusion from apatite: General behavior as illustrated by Durango fluorapatite: Journal of Geophysical Research, 105, 2903–2914.

Farley, K.A., and Stockli, D.F., 2002, (U-Th)/He dating of phosphates: apatite, monazite, and xenotime, in Phosphates: Geochemical, Geobiological, and Materials Importance, Rev. Mineral. Geochem., vol. 48, 559-577.

Fitzgerald, P.G., Baldwin, S.L., Webb, L.E., and O'Sullivan, P.B., 2006, Interpretation of (U-Th)/He single grain ages from slowly cooled crustal terranes: A case study from the Transantartic Mountains of southern Victoria Land: Chemical Geology, 225, 91-120.

House, M.A., Wernicke, B.P., Farley, K.A., and Dumitru, T.A., 1997, Cenozoic thermal evolution of the central Sierra Nevada from (U-Th)/He thermochronometry: Earth Planet. Sci. Lett., 151, 167-179.

Mancktelow, N.S., and Grasemann, B., 1997, Time-dependent effects of heat advection and topography on cooling histories during erosion, Tectonophysics, 270, 167-195.

Mayo, L.R., 1986, Annual runoff rate from glaciers in Alaska: A model using the altitude of glacier mass balance equilibrium, in D.L. Kane (ed.), Cold Regions Hydrology Symposium, Amer. Water Res. Assoc., Bethesda, Maryland, 509-517.

McDowell, F.W., Mclntosh, W.C., and Farley, K.A., 2005, A precise $^{40}Ar/^{39}Ar$ reference age for the Durango apatite (U-Th)/He and fission-track dating standard: Chemical Geology, 214, 249-263.

Meierding, T.C., 1982, Late Pleistocene glacial equilibrium-line altitudes in the Colorado front range: A comparison of methods, Quat. Res., 18, 289-310.

Meigs, A., and Sauber, J., 2000, Southern Alaska as an example of the long-term consequences of mountain building under the influence of glaciers, Quat. Sci. Reviews, 19, 1543-1562.

Péwé, T.L., 1975, Quaternary geology of Alaska, U.S. Geol. Surv. Professional Paper, 835, 139 p.

Porter, S.C., 1989, Late Holocene fluctuations of the fjord glacier system in Icy Bay Alaska, Arctic and Alpine Research, 21, 364-379.

Reiners, P.W., and Brandon, M.T., 2006, Using thermochronology to understand orogenic erosion, Ann. Rev. Earth and Planet. Sci., 34, 419-466.

Reiners, P.W., and Nicolescu, S., in press, Measurement of parent nuclides for (U-Th)/He chronometry by solution sector ICP-MS, Geochim. Cosmochim. Acta.

Roe, G. and O'Neal, M.A., in prep., The response of glaciers t intrinsic climate variability: observations and models of late Holocene variations in the Pacific Nothwest, J. Glaciology.

Spatial Climate Analysis Center, 2002, PRISM 1961-1990 Mean Annual Precipitation: Alaska, Oregon Climate Service, Oregon State University, via The Climate Source, http://www.cimatesouce.com/ak/fact_sheets/akppt_xl.jpg.

Spotila, J.A., Buscher, J., Meigs, A., and Reiners, P., 2004, Long-term glacial erosion of active mountain belts: Example of the Chugach-St. Elias Range, Alaska, Geology, 32, 501-504.

Wolf, R.A., Farley, K.A., and Silver, L.T., 1996, Helium diffusion and low-temeprature thermochronometry of apatite, Geochim. Cosmochim. Acta, 60, 4231-4240.

FIGURE CAPTIONS

Figure DR-1: Vertical AHe transect at Khitrov ridge, just west of the Bering glacier. The samples represented are (from highest to lowest) 05STP3, 05STP1, and 05STP2 (Fig. 1). Individual age determinations are shown as triangles, whereas the average age for each sample is shown as a large circle. Error bars for the average ages are given for the standard deviation of individual analyses (1σ). The regression is based on the three average ages, rather than on all individual age determinations, with age as the dependent variable. Regression equation shown at bottom right.

Figure DR-2: Glacier drainage basins of the St. Elias orogen, overlain on shaded relief map from USGS 60-m DEMs. Glacier basins were mapped using 1:250,000 scale topographic maps, based on the elevation of the glacier surface and direction of the ice-surface gradient (*cf.* Mayo, 1986). Only glaciers that drain southwards or eastwards are shown; smaller glaciers on the leeward flank of the range are not plotted. ELAs of each glacier are shown as the bright blue lines and were determined based on the boundary

between concave (above ELA) and convex (below ELA) ice contours (*cf.* Péwé, 1975). The names, drainage areas, and ELAs of each numbered glacier are listed in Table DR-2. Two sets of isohyets of mean annual precipitation (cm/yr) are shown. Those in black are from the regional climate summary of Péwé (1975). Those in blue are from PRISM model of recent precipitation data (Spatial Climate Analysis Center, 2002). Line AA' indicates profile used to construct Fig. 2.

Figure DR-3: West to east profile of Waxell-St. Elias ridge (BB', Fig. 1). Maximum elevation along the circuitous ridge line is from 1:250,000 scale maps. The ridge is comprised of four elliptical sections (dashed lines) separated by outlet glaciers. Height of the modern surface of the Bagley ice field to the north is shown as heavier dashed line. Ice currently cuts through the ridge at only five locations (denoted by stars), and may have flowed over the ridge during glacial maxima at three additional spots (denoted by circles).

Table DR-1: AHe data.

Sample	Elev. (m)	Latitude	Longitude	Lithology	# Grains	Mass (mg)	Ft	U ppm	Th ppm	MWAR	He pmol	Age (Ma)	Avg. (Ma)	% SD
05STP1-1	946	60.4208°	-143.5028°	arkose	7	0.0311	0.796	23.5	36.9	63.0	0.0019	**0.45**	**0.53±0.07**	±14.2%
-2				(Kulthieth)	8	0.0526	0.820	25.3	26.4	77.8	0.0048	**0.67**		
-3					8	0.0323	0.767	22.6	31.3	61.1	0.0021	**0.55**		
-4					8	0.0603	0.826	24.1	7.85	81.8	0.0036	**0.54**		
-5					4	0.0419	0.838	6.28	6.82	82.4	0.0007	**0.50**		
-6					4	0.0320	0.837	15.4	31.0	85.6	0.0014	**0.45**		
05STP2-1	620	60.3931°	-143.5422°	arkose	16	0.0377	0.743	25.0	36.6	51.9	0.0019	**0.39**	**0.44±0.03**	±6.9%
-2				(Kulthieth)	15	0.0342	0.736	41.1	42.3	50.6	0.0029	**0.43**		
-3					16	0.0455	0.759	37.6	60.0	55.3	0.0043	**0.46**		
-4					11	0.0403	0.771	34.6	21.1	61.7	0.0030	**0.47**		
-5					13	0.0487	0.777	33.5	23.9	60.6	0.0036	**0.47**		
05STP3-1	1252	60.4332°	-143.5044°	arkose	14	0.0446	0.755	29.0	29.8	54.5	0.00041	**0.64**	**0.53±0.10**	±19.6%
-2				(Kulthieth)	7	0.0569	0.823	37.1	29.1	84.9	0.0070	**0.65**		
-3					12	0.0458	0.866	17.7	17.7	59.2	0.0018	**0.39**		
-4					9	0.0435	0.798	39.5	46.2	71.0	0.0040	**0.44**		
-6					3	0.0211	0.836	15.2	22.4	79.2	0.0010	**0.55**		
05STP4-1	394	60.3896°	-143.6997°	arkose	6	0.0411	0.830	10.1	16.2	74.4	0.0021	**0.86**	**0.74±0.07**	±9.7%
-2				(Kulthieth)	6	0.0341	0.803	22.5	30.4	65.8	0.0031	**0.73**		
-3					5	0.0416	0.819	58.2	64.4	76.0	0.0093	**0.72**		
-4					5	0.0391	0.825	28.5	25.9	74.2	0.0046	**0.78**		
-5					6	0.0556	0.837	11.6	15.1	82.3	0.0023	**0.62**		
-6					6	0.0559	0.827	46.1	38.1	77.4	0.0100	**0.75**		
05STP7-1	1140	60.8838°	-143.7637°	gneiss	6	0.0380	0.810	95.2	2.3	72.7	0.3984	**25.9**	**25.1±0.87**	±3.5%
-2				(Chugach)	4	0.0270	0.832	100.5	0.6	78.1	0.2982	**25.3**		
-3					5	0.0201	0.777	109.3	0.6	57.9	0.2269	**25.4**		
-4					10	0.0142	0.728	75.3	1.0	42.2	0.0962	**23.6**		
05STP11-1	1448	60.5428°	-143.4165°	sandstone	5	0.0157	0.765	36.0	28.6	56.0	0.0463	*17.3*	**1.78±0.83**	±46.7%
-2				(Orca Group)	13	0.0146	0.678	61.0	36.0	38.0	0.0103	**2.86**		
-3					15	0.0164	0.675	43.8	36.2	39.9	0.0050	**1.64**		
-4					15	0.0164	0.658	22.6	26.2	40.8	0.0014	**0.84**		
05STP15-1	488	60.2306°	-143.9758°	sandstone	15	0.0278	0.715	23.6	26.6	46.7	0.0055	**1.76**	**1.80±0.11**	±6.1%
-2				(Poul Creek)	1	0.0212	0.895	1.97	6.52	101.2	0.0080	*22.8*		
-3					16	0.0287	0.726	28.0	35.9	49.3	0.0069	**1.72**		
-4					16	0.0307	0.728	29.1	29.2	46.9	0.0105	*2.47*		
-5					10	0.0222	0.723	13.5	13.1	47.2	0.0028	**1.99**		
-6					10	0.0204	0.728	46.0	26.8	48.2	0.0071	**1.74**		
-7					1	0.0265	0.884	2.17	7.24	105.8	0.0130	*2.71*		

Table DR-1: cont.

Sample	Elev. (m)	Latitude	Longitude	Lithology	# Grains	Mass (mg)	Ft	U ppm	Th ppm	MWAR	He pmol	Age (Ma)	Avg. (Ma)	% SD
05STP26-1	2208	60.6469°	-143.7903°	granite	16	0.0218	0.706	111	0.7	42.5	0.0190	**2.14**	**2.28±0.16**	±6.9%
-2				(Chugach)	14	0.0184	0.690	104	0.4	42.0	0.0142	**2.06**		
-3					11	0.0205	0.728	98.3	1.0	50.1	0.0179	**2.35**		
-4					5	0.0192	0.794	135	0.9	61.5	0.0239	**2.23**		
-5					2	0.0173	0.828	112	1.6	71.2	0.0212	**2.54**		
-6					4	0.0285	0.831	114	1.1	76.5	0.0331	**2.36**		
05STP27-1	1704	60.4996°	-143.7248°	arkose	15	0.0166	0.665	34.2	53.8	39.4	0.0017	**0.63**	**0.63±0.11**	±17.5%
-2				(Kulthieth)	12	0.0176	0.700	36.5	41.4	41.5	0.0022	**0.74**		
-3					19	0.0186	0.670	39.1	43.4	36.6	0.0024	**0.76**		
-4					7	0.0191	0.787	19.3	33.1	56.0	0.0010	**0.46**		
-5					10	0.0217	0.727	31.8	55.3	47.4	0.0021	**0.57**		
05STP33-1	2758	60.6441°	-143.7239°	granite	7	0.0584	0.850	66.4	23.9	78.4	0.0334	**1.79**	**1.66±0.09**	±5.6%
-2				(Chugach)	6	0.0623	0.845	73.2	27.6	84.8	0.0334	**1.53**		
-3					10	0.0743	0.831	67.6	25.2	75.7	0.0379	**1.60**		
-4					9	0.0454	0.816	71.1	27.5	64.9	0.0238	**1.58**		
-5					3	0.0363	0.859	69.2	20.2	92.5	0.0206	**1.70**		
-6					4	0.0296	0.826	76.0	26.7	76.2	0.0183	**1.74**		
06STP1-1	1189	60.1686°	-140.5297°	sandstone	16	0.0255	0.717	44.5	61.5	44.3	0.0094	**1.65**	**1.55**	>20%
-2				(Poul Creek/	8	0.0290	0.771	32.2	37.4	58.2	0.0267	*5.54*		
-3				Yakataga)	8	0.0226	0.753	34.4	44.0	52.3	0.0058	**1.45**		
-4					16	0.0216	0.714	29.4	33.2	43.5	0.0145	*4.82*		
-5					16	0.0235	0.721	39.2	39.2	43.8	0.0402	*8.78*		
06STP3-1	1713	60.1643°	-140.3476°	sandstone	17	0.0254	0.730	44.0	40.7	47.4	0.0386	**7.41**	**7.21±1.16**	±16.1%
-2				(Poul Creek)	12	0.0201	0.724	26.5	35.9	47.7	0.0225	**8.41**		
-3					4	0.0146	0.759	40.0	41.3	55.5	0.4309	*148*		
-4					4	0.0110	0.743	15.0	12.2	50.1	0.0041	**5.30**		
-5					7	0.0238	0.753	59.6	17.8	56.2	07314	*122*		
-6					15	0.0123	0.645	45.7	52.5	35.9	0.0187	**7.72**		
-7					10	0.0138	0.733	33.6	20.7	47.6	0.0275	*13.5*		
06STP4-1	1676	60.2369°	-140.4611°	quartzite	14	0.0204	0.713	13.5	16.2	45.0	0.00038	*1.44*	**0.56±0.08**	±15.3%
-2				(Orca Group)	18	0.0207	0.680	28.3	38.1	39.1	0.00031	**0.59**		
-3					10	0.0154	0.703	6.3	18.0	44.5	0.00007	**0.44**		
-4					11	0.0130	0.699	47.4	55.3	41.4	0.00161	*1.80*		
-5					11	0.0130	0.684	26.0	30.9	39.4	0.00031	**0.64**		
06STP50-1	875	60.4488°	-143.9837°	sandstone	19	0.0244	0.678	55.0	54.1	40.3	0.0060	**1.02**	**1.09±0.09**	±8.3%
-2				(Kulthieth)	18	0.0221	0.684	48.6	63.6	39.6	0.0062	**1.23**		
-3					19	0.0254	0.689	46.0	56.9	40.6	0.0054	**1.00**		
-4					19	0.0247	0.691	45.4	53.5	39.7	0.0056	**1.09**		

Table DR-1: cont.

Sample	Elev. (m)	Latitude	Longitude	Lithology	# Grains	Mass (mg)	Ft	U ppm	Th ppm	MWAR	He pmol	Age (Ma)	Avg. (Ma)	% SD
06STP71-1	853	60.1333°	-140.7119°	sandstone	10	0.0230	0.752	38.2	26.4	53.5	0.0215	**5.35**	**3.95±1.06**	±26.8%
-2				(Yakataga)	8	0.0169	0.738	52.3	30.8	49.6	0.0145	**3.73**		
-3					7	0.0151	0.744	91.1	104	48.6	0.0577	*8.47*		
-4					13	0.0292	0.733	45.6	36.5	50.8	0.0169	**2.78**		
-5					6	0.0173	0.769	29.9	18.5	55.3	0.0193	*8.08*		
01CH22-1	1532	60.9104°	-144.3150°	schist	11	0.0077	0.637	33.3	17.8	33.1	0.0194	**20.1**	**18.9±1.20**	±6.3%
-2				(Chugach)	12	0.0035	0.521	38.6	17.3	25.7	0.0072	**17.7**		
01CH25-1	320	60.6940°	-144.3774°	phyllite	20	0.0171	0.662	116.8	16.7	36.4	0.0708	**9.92**	**10.7±1.31**	±12.3%
-2				(Chugach)	2	0.0068	0.750	50.3	6.9	56.7	0.0134	**9.71**		
-3					20	0.0174	0.658	108.1	10.6	36.5	0.0695	**10.5**		
-4					13	0.0204	0.710	65.8	4.0	46.4	0.0515	**10.2**		
-5					8	0.0130	0.715	67.6	30.6	42.4	0.0716	*19.7*		
-6					12	0.0222	0.738	92.8	12.9	51.9	0.1092	**13.3**		
01CH26-1	884	60.4990°	-144.4772°	granitoid	4	0.0103	0.797	24.0	15.0	55.5	0.0021	**1.79**	**2.02±0.14**	±7.2%
-2				(Chugach)	5	0.0095	0.751	32.0	18.8	50.3	0.0028	**2.04**		
-3					6	0.0170	0.752	30.3	16.8	54.3	0.0050	**2.19**		
-4					7	0.0176	0.748	30.3	18.5	51.2	0.0049	**2.06**		
02CH28-1	1625	60.2573°	-141.1584°	graywacke	12	0.0217	0.704	14.9	19.3	49.5	0.0034	*2.19*	**0.74±0.14**	±18.7%
-2				(Kulthieth)	15	0.0234	0.691	18.3	30.1	46.2	0.0012	**0.55**		
-3					11	0.0242	0.721	19.2	16.6	54.2	0.0018	**0.87**		
-4					14	0.0243	0.718	17.5	19.0	47.9	0.0016	**0.81**		

Ages in italics were considered outliers and not used for average age calculation
Elev. (m) – sample elevation
Ft – alpha ejection correction after Farley et al. (1996)
MWAR – mass weighted average radius of sample (μm)
Avg. – average AHe age (Ma)
% SD – standard deviation of average age as percentage of the average age
Chugach = Chugach terrane. Yakataga, Poul Creek, and Kulthieth are formations in the Yakutat terrane. Orca Group is a formation in the Prince William terrane.

Table DR-2: Glacier data.

#	Glacier	ELA (m)	Drainage Area (km^2)	Exhumation Rate (mm/yr)
1	"Martin River West"	732	43	2.0
2	Miles	1006	135	1.5
3	"Mt. Tom White"	1341	20	1.5
4	Martin River	853	176	2.5
5	Fan	1372	65	2.5
6	"Martin River East"	1036	42	3.0
7	Stellar	671	575	5.0
8	"Khitrov"	853	51	4.0
9	"Mt. Stellar A"	1036	20	3.0
10	"Mt. Stellar B"	975	8	3.0
11	"Mt. Stellar C"	914	8	3.0
12	"Mt. Stellar D"	914	9	2.7
13	"Mt. Stellar E"	1036	36	2.7
14	"Mt. Stellar F"	975	24	2.7
15	Bering	1128	2516	3.0
16	Leeper	732	30	3.3
17	Yakataga	914	49	2.0
18	Yaga	914	24	1.5
19	White River	762	22	1.5
20	Guyot	671	397	2.5
21	Yhatse	610	1109	2.7
22	Tyndall	701	166	2.8
23	Libby	792	75	2.5
24	Agassi	853	308	2.5
25	Seward	914	1949	4.0
26	"Marvine West"	823	27	2.0
27	Marvine	823	115	2.0
28	Hayden	732	55	2.0
29	Turner	792	124	2.0
30	Valerie	853	272	2.0
31	"Mt. Foresta"	1097	23	2.0
32	Hubbard	732	3406	2.7

- refer to glaciers numbered in Figure 2, from west to east.

Glacier - glacier names are from 1:250,000 USGS topographic maps; those in parentheses have no official name.

ELA – equilibrium line altitude; measured based on contour shape on 1:250,000 USGS topographic maps in feet, converted to meters.

Drainage Area – measured graphically based on ice divides following ice surface gradients from 1:250,000 USGS topographic maps.

Exhumation Rate – based on contours on Figure 1.

Figure DR-1

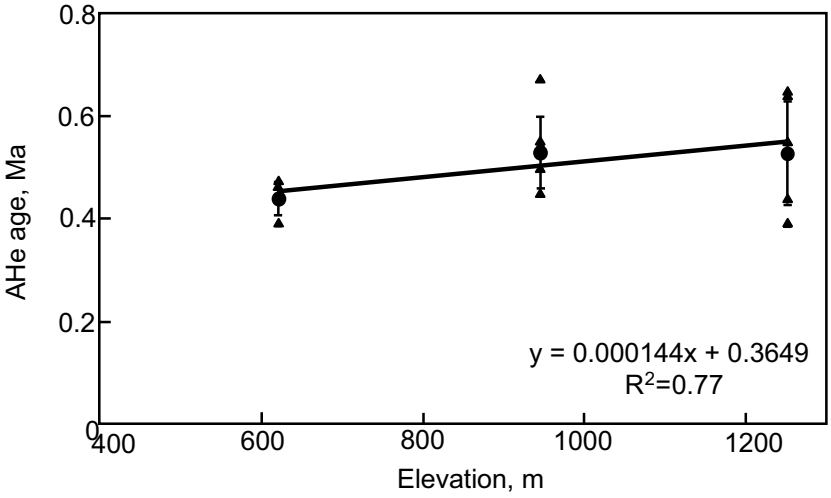
0.8
0.6
0.4
0.2
0
AHe age, Ma
400
600
800
1000
1200
Elevation, m
y = 0.000144x + 0.3649
R2=0.77

Figure DR-2

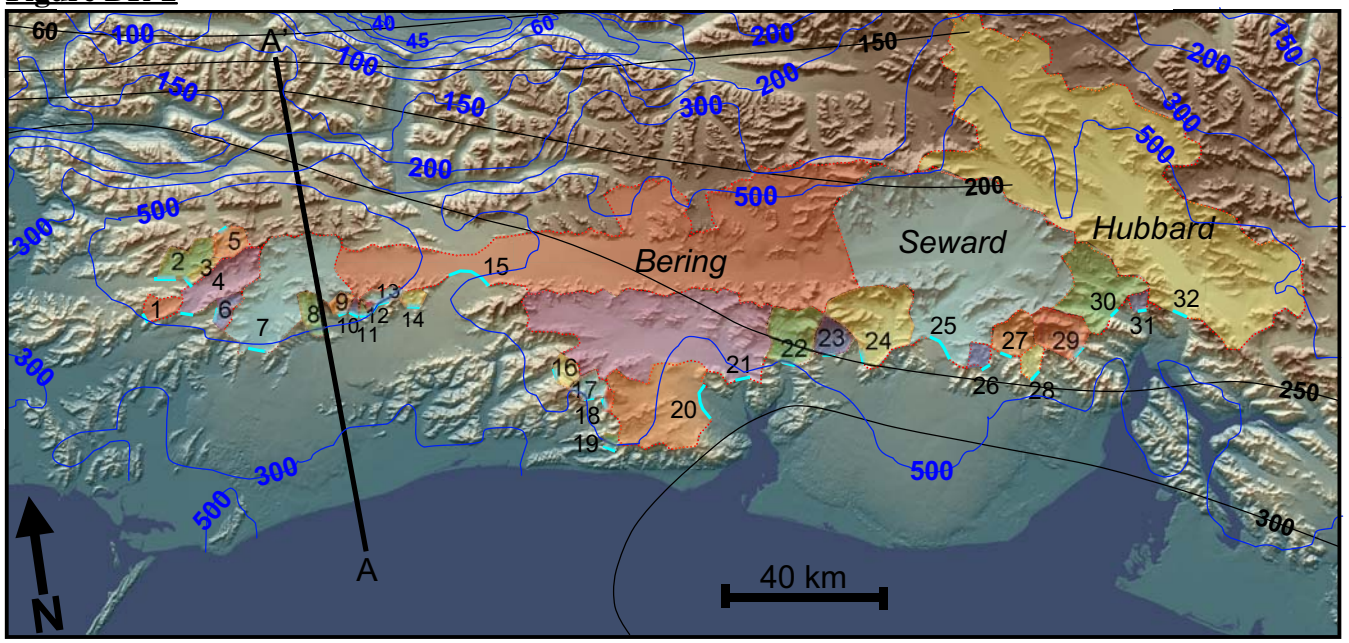
A'
A
Bering
Seward
Hubbard
N
40 km
60
100
150
200
300
500
40
45
250

Figure DR-3

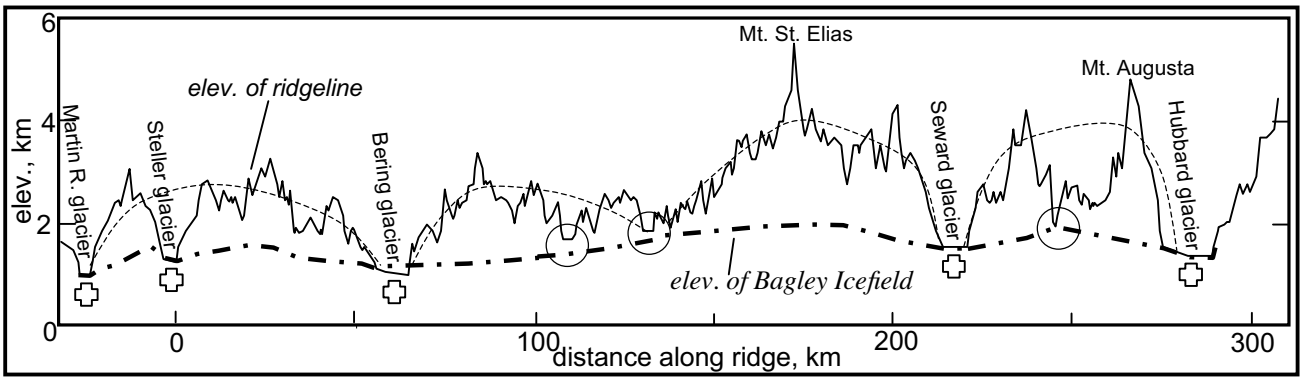
6
4
2
0
elev., km
Mt. St. Elias
Mt. Augusta
elev. of ridgeline
Martin R. glacier
Steller glacier
Bering glacier
Seward glacier
Hubbard glacier
elev. of Bagley Icefield
0
100
200
300
distance along ridge, km